J Mater Sci (2020) 55:524–534

Ceramics

Microscopic mapping of dopant content and its link to the structural and thermal stability of yttria-stabilized zirconia polycrystals

Wenliang Zhu[1,*], Shizuka Nakashima[1], Elia Marin[1], Hui Gu[2], and Giuseppe Pezzotti[1,3,4,5,*]

[1] Ceramic Physics Laboratory, Kyoto Institute of Technology, Sakyo-ku, Matsugasaki, Kyoto 606-8585, Japan
[2] Department of Materials Science and Engineering, Shanghai University, Shanghai, People's Republic of China
[3] Department of Orthopaedic Surgery, Tokyo Medical University, 6-7-1, Nishi-Shinjuku, Shinjuku-ku, Tokyo 160-0023, Japan
[4] The Center for Advanced Medical Engineering and Informatics, Osaka University, Yamadaoka, Suita, Osaka 565-0871, Japan
[5] Department of Immunology, Graduate School of Medical Science, Kyoto Prefectural University of Medicine Kamigyo-ku, 465 Kajii-cho, Kawaramachi dori, Kyoto 602-0841, Japan

Received: 27 August 2019
Accepted: 22 September 2019
Published online: 1 October 2019

ABSTRACT

The effect of yttria content on structural and thermal stability of zirconia in yttria-stabilized zirconia (YSZ) polycrystalline ceramics was systematically investigated by Raman spectroscopy and X-ray photoelectron spectroscopy. Taking advantage of an experimentally retrieved linear dependence of Raman bandwidth on yttria content, Raman imaging was applied as an effective tool in examining the local yttrium distribution in YSZ ceramics and its relationship with environmentally driven polymorphic transformation. A significant variation of monoclinic fraction with yttria content and temperature was found and interpreted according to a newly proposed model, which takes into account the change in lattice hydroxyl and oxygen vacancies and the possible formation of stable defect complexes.

Introduction

Superior mechanical properties (e.g., high strength and toughness) make polycrystalline yttria-stabilized zirconia (YSZ) suitable for a wide field of applications as a structural ceramic. Its outstanding biocompatibility and high esthetic potential has made it the material choice in dental application [1–3]. Recently, it has attracted much attention for applications as electrolyte membrane and as a component in composite cathodes or cermet anodes for solid oxide fuel cells (SOFCs) through the exploitation of its high corrosion resistance, high ionic conductivity, and low thermal conductivity [4–6]. However, these properties of YSZ ceramics may be degraded by phase instability in the service environments (e.g., humidity and temperature).

Address correspondence to E-mail: wlzhu@kit.ac.jp; pezzotti@kit.ac.jp

https://doi.org/10.1007/s10853-019-04080-9

It is long known that low-temperature degradation of the material performance is induced by the tetragonal-to-monoclinic polymorphic transformation that occurs in YSZ doped with low content yttria (< 8 mol%), when exposed to biological or hydrothermal environments [7–11]. 8–9 mol% YSZ for SOFCs applications appear to be situated in the 2-phase field (cubic + tetragonal) of the YSZ phase diagram at the working temperatures, which causes material's decomposition into Y-enriched and depleted regions on the nm-scale. Such decomposition in turn induces an electrical degradation (i.e., a lowered ionic conductivity) during operation [12]. Such undesirable aspect of environmentally dependent polymorphism in zirconia ceramics has been found dependent on the selection of sintering additives, dopant content, and process control including proprietary methods unique to each manufacturer [7, 13–17].

In general, grain size and grain boundary composition is taken to interplay with water and/or water molecular and to control the kinetics of degradation [18]. Recently, we have revealed various kinetics of zirconia polymorphic transformation in different environments and the critical roles played by oxygen vacancy and surface and lattice hydroxyl defects due to the occurrence of distinct off-stoichiometric chemistry, including hydroxylation, hydroxyl migration, surface reconstruction, and dehydroxylation during hydrothermal/thermal treatments [19, 20].

Because of the stabilization effect of the Y dopant, the variation of Y/Zr ratio inside the grains for a low-content Y-doped ceramic indicates different probabilities of phase transformation even neglecting other factors. Consequently, a quantitative visualization of yttrium content and its distribution as well as its influence on the phase stability could be useful for understanding the entire material stability.

In this paper, the effect of yttria content on the structure and the thermal stability of zirconia in YSZ samples were systematically investigated by Raman and X-ray photoelectron spectroscopies (XPS) and X-ray diffraction. A series of YSZ samples doped with different yttria contents were subjected to thermal treatments at different temperatures. A linear dependence of the bandwidth of the 146 cm^{-1} tetragonal band on yttria content at different temperatures was observed, enabling to develop a Raman imaging algorithm effective in examining local yttrium distribution in YSZ ceramics. A significant variation in monoclinic volume fraction, V_m, of zirconia was found with changing yttria content and temperature, which was interpreted by a model taking into account a change in lattice defects.

Experimental procedures

The samples investigated in this research included a series of zirconia stabilized by 3, 4, 6, 8, and 10 mol% yttria, respectively (henceforth simply referred to as *X*YSZ, where *X* is the molar percent of yttria). These samples were fabricated from the raw powders (average grain size of about 0.2 μm) according to a hot isostatic pressing cycle (for 1 h at 1350 °C) following pressureless sintering (at 1350 °C) to achieve full density. The sample storage was similar to that described in Ref. [20]. The grain size of the fabricated ceramics varied in the range from 100 to 700 nm, with an averaged value of about 400 nm (cf. scanning electron microscope graph and histograms of grain size shown in Fig. S1(a) and (b) in supplementary material). The fabricated samples were cut into a number of smaller pieces and then some of these pieces were concurrently subjected to in vitro isothermal treatments in a conventional electric heater (NHK-120BS-II, Nitto Kagaku Co.) operating at 300, 500, and 700 °C in air for 12 h, respectively.

Raman spectroscopic analyses were comparatively performed at room temperature (RT) before and after thermal treatments using a single monochromator (T-64000, Jobin-Ivon/Horiba Group, Kyoto, Japan). Raman mappings of 100 × 100 μm^2 with a step of 10 μm were conducted on the samples to obtain respective average spectra.

X-ray photoelectron spectroscopy (XPS) experiments were performed on the top surfaces of these samples by using a photoelectron spectrometer (JPS-9010 MC; JEOL Ltd., Tokyo, Japan). The monochromatic MgKα line was used as the X-ray source in this study (output 10 kV, 10 mA). The measurements were conducted in a vacuum chamber at around 2×10^{-7} Pa, upon setting the analyzer pass energy to 10 eV and the voltage step size to 0.1 eV. The incident angle of the X-ray and the takeoff angle were 34° and 90°, respectively.

X-ray diffraction analyses of the YSZ samples were performed on Rigaku Miniflex 600 system (Rigaku

Corporation, Tokyo, Japan), using the CuKα radiation (40 kV and 15 mA).

Results

Raman spectroscopy

Figure 1a shows a comparison of the Raman spectra of the YSZ samples. As can be seen, the YSZ samples doped with yttria less than 8 mol% consisted of both tetragonal and monoclinic phases (cf. peculiar bands to these phases labeled in inset as *t* and *m*, respectively), while the 8YSZ and 10YSZ samples displayed the Raman bands of cubic and tetragonal zirconia (cf. strongest and broadest band at 610 cm^{-1} for cubic ZrO_2 versus strong band at 640 cm^{-1} for *t*-ZrO_2). Upon thermal treatments, all the YSZ ($X < 8$ mol%) samples showed a gradual reduction in the monoclinic peak intensities with increasing temperature (Fig. 1b–d), with respect to that of the 145 cm^{-1} tetragonal band, while no marked changes in the spectral morphology could be found in the 8YSZ and 10YSZ samples when subjected to any of the thermal treatment applied in this study.

Figure 2 shows comparative results of Raman mapping experiments on the 3YSZ, 4YSZ, and 6YSZ samples (also cf. supplementary material, Fig. S2): (a) maps of monoclinic volume fraction, V_m, collected with focusing at the surface of the YSZ samples before thermal treatment are shown (as calculated according to the Katagiri equation from the tetragonal band labeled *t* at 145 cm^{-1} and the monoclinic doublet *m* bands at 176 and 188 cm^{-1} [21]) and (b) average values for the samples subjected to thermal treatments at different temperatures. As can be seen, with increasing yttria content from 3 to 6 mol%, the RT V_m value gradually decreased from ~ 56 to ~ 40%. Exposures of 3–6YSZ samples to thermal environments (up to 700 °C) gradually reduced the content of monoclinic polymorph; the higher the yttria content, the lower the V_m content at each temperature.

In addition, clear dependences of spectral position and full width at half maximum (FWHM) of the *t* band at 145 cm^{-1} and the *m* band at 176 cm^{-1} on both yttria content and thermal treatment temperature could be observed for the above three selected YSZ samples, as shown in Fig. 3. With increasing yttria content, the peak position of the 145 cm^{-1}

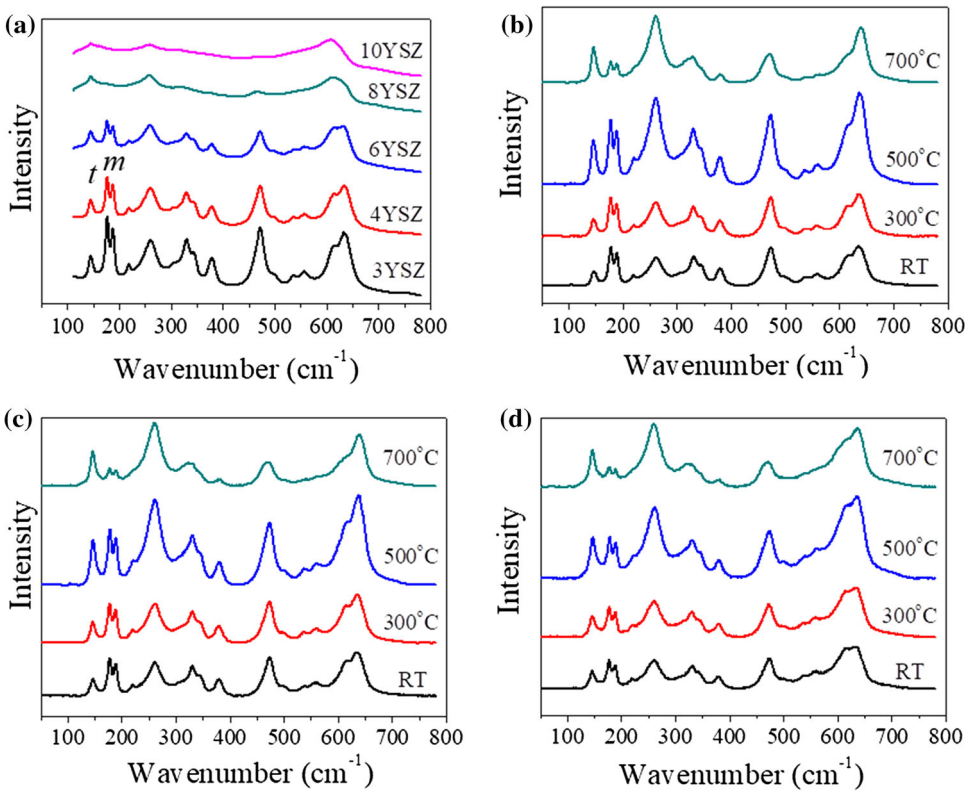

Figure 1 Average Raman spectra of **a** all YSZ samples before thermal treatment, and those of **b** 3YSZ, **c** 4YSZ, and **d** 6YSZ samples treated at different temperatures. The symbols of *t* and *m* represent Raman bands of *t*-ZrO_2 and *m*-ZrO_2, respectively.

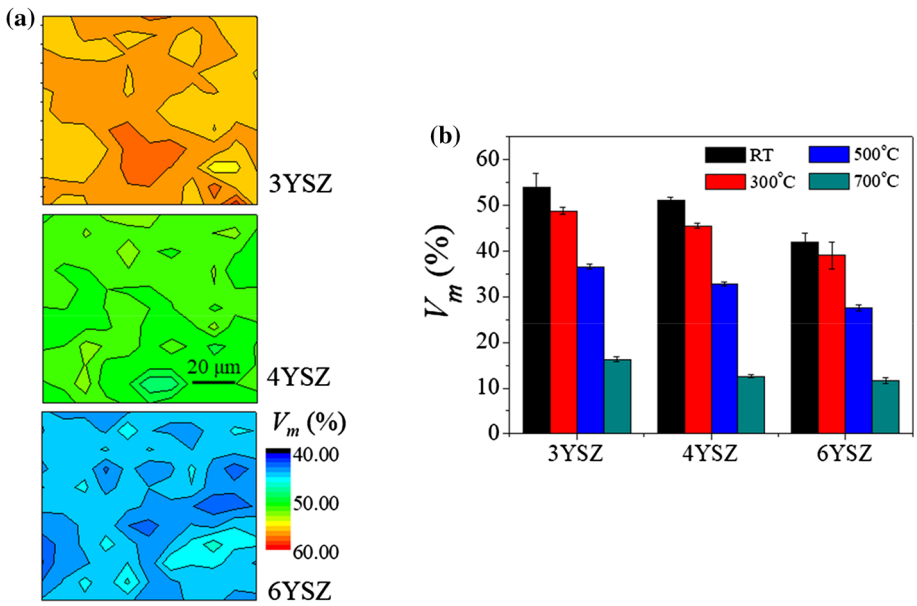

Figure 2 **a** Maps of monoclinic fraction, V_m for untreated 3YSZ, 4YSZ, and 6YSZ samples, and **b** statistically validated V_m values for the YSZ samples before and after thermal treatments at different temperatures.

tetragonal band showed a shift to higher wave numbers together with a concurrent tendency to band broadening, while the 176 cm^{-1} monoclinic band exhibited a negligible shift and a slight band narrowing. When temperature increased, both bands showed a clear shift of their position to higher wave numbers in all the samples. However, unlike the band broadening observed for the tetragonal phase in response to temperature increase, the monoclinic band exhibited a reduction in its FWHM when temperature rose up.

Note that in the case of doping with low content yttria, a certain amount of cubic phase can exist in the YSZ ceramics. In this research, the YSZ samples did not contain any di-valence ions and were sintered at sufficiently low temperature to avoid the occurrence of a dual cubic–tetragonal microstructure [22]. Accordingly the presence of a fraction of cubic phase can be considered negligible. In order to examine the hypothesis, X-ray diffraction analyses were conducted on the YSZ samples without thermal treatments.

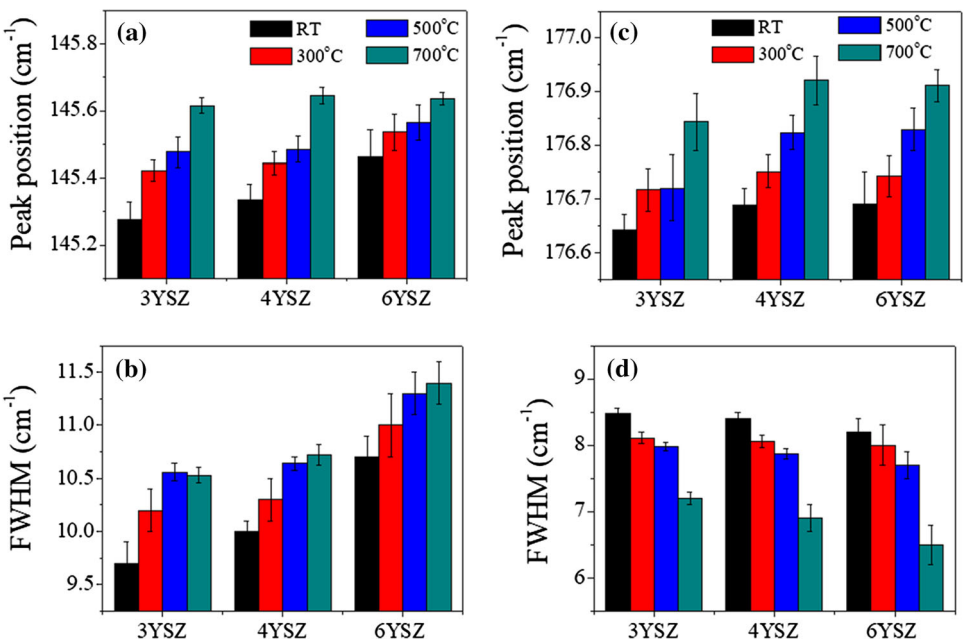

Figure 3 Variations of **a**, **c** peak position and **b**, **d** FWHM of the tetragonal 145 cm^{-1} (**a**, **b**) and the monoclinic 176 cm^{-1} (**c**, **d**) Raman bands for 3–6YSZ samples before and after thermal treatments at different temperatures.

X-ray diffraction

Figure 4a shows a comparison of the X-ray diffraction patterns of the YSZ samples. The samples doped with low Y content (< 8 mol%) show two peaks arising from monoclinic zirconia phases at about 28.2° and 31.4° for 2θ, and one intense peak at 30.19° assigned to the tetragonal phase of zirconia, while the samples of high doping (≥ 8YSZ) exhibit only one strong peak located at the 2θ angle of around 30.09°, attributed to the cubic phase. Spectral deconvolution of these peaks was then carried out by using Lorentz function, revealing a resolvable single peak arising from tetragonal and cubic phases, respectively, for the intense peak at 30.1°, with the results also shown in Fig. 4a. As the content of yttria in YSZ increases, the monoclinic peaks gradually become weak until they disappear upon high content doping. In the meanwhile, with increasing yttria content, the peak position of the tetragonal phase shows a linear shift to lower angles to approach that of the cubic phase (cf. Fig. 4b). A deviation from the linear shift could be observed when the dopant content is higher than 8 mol%. Similarly, the full width at half maximum of the peak also exhibits a linear reduction in response to the dopant increase upon low doping, while no more band narrowing (or even a slight increase) could be found in the case of very high yttria doping (i.e., 10YSZ) (Fig. 4c). The results indicate a gradual reduction of tetragonality with the addition of yttria in zirconia to retain a cubic structure upon doping with yttria higher than 8 mol%.

Note that here only one strong peak was considered for the samples with high doping (≥ 8YSZ), attributed to the cubic phase. However, as shown in Fig. 1a, the 8YSZ and 10YSZ samples also exhibited the Raman bands of tetragonal-like zirconia (146 and 260 cm^{-1}). This probably was induced by the imperfection of lattice distortion (e.g., generation of Y_{Zr}–V_o–Y_{Zr} defect complexes, as will be discussed later) upon heavy doping and/or the presence of a small amount of tetragonal phase due to an inhomogeneous distribution of yttrium in zirconia and the relatively low sintering temperature according to the phase diagram of YSZ [23, 24]. Because of the difference in the Raman scattering cross section between tetragonal and cubic phases, as well as in the probe sensitivity between XRD analysis and Raman spectroscopy, such imperfection can be revealed by the molecular-vibration sensitive Raman scattering.

XPS spectroscopy

In order to further investigate the structural alteration induced by yttria doping, XPS measurements were then carried out on these YSZ samples. Figure 5 shows the variations of Zr3*d*, Y3*d*, and O1*s* XP spectra for the 3–6YSZ samples. The two main peaks in the Zr3*d* (Y3*d*) XP spectra originate from Zr3$d_{5/2}$ (~ 182 eV) and Zr3$d_{3/2}$ (~ 184 eV) in Zr–O bonds

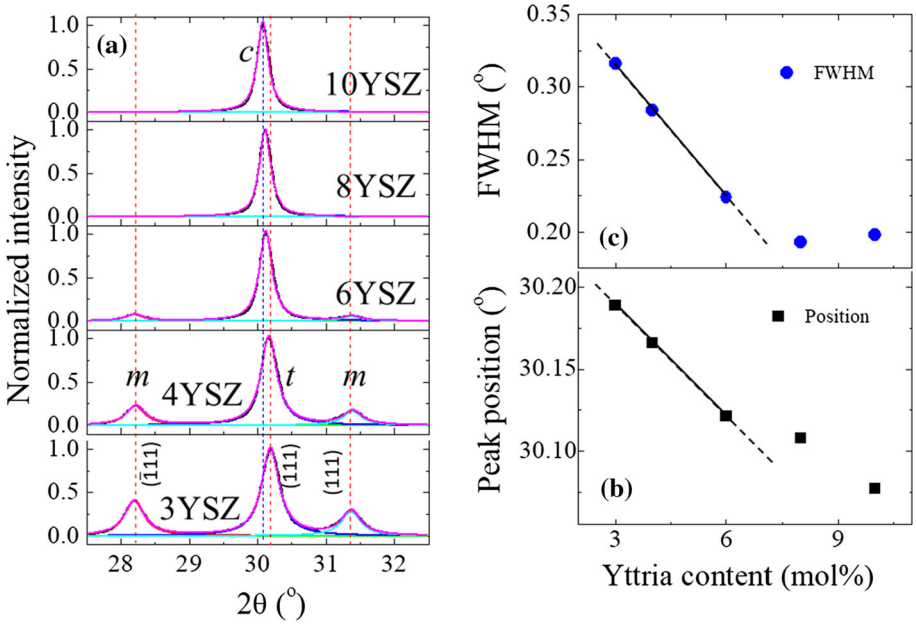

Figure 4 Variations of **a** X-ray diffraction patterns, **b** peak position, and **c** FWHM of the tetragonal/cubic peak with yttria content in YSZ. The solid and dashed lines in (**b**) and (**c**) show the presence and extension of respective linear relationships.

(Y3$d_{5/2}$ and Y3$d_{3/2}$ in Y–O bonds), and the two broad peaks in the O1*s* spectra are attributed to O–Zr(Y) (~ 530 eV) and O–H (~ 532 eV), respectively. A clear shift of the peak positions to higher binding energies with increasing yttria content could be observed. According to previous studies [19, 20], for low doping, two and four Gaussian sub-bands can be applied for spectral deconvolution of each main Zr3*d* (Y3*d*) peak and the O1*s* peak, respectively, considering the different binding energies of Zr–O (Y–O) and O–H between monoclinic and tetragonal phases. In the case of cubic 10YSZ, only one and two sub-bands are applied for these peaks. Note that here for simplicity we neglected the nuanced difference in binding energy between O–Zr and O–Y for deconvoluting the O1*s* spectra. The results of the fitting procedures are shown in Fig. 5 with detailed peak identification and related fractions given in Fig. 6a–c. The Zr3*d*, Y3*d* and O1*s* XP peaks of the samples revealed contributions from Zr–O binding and O–Zr and O–H clusters in both tetragonal (peaks 2 and 4, II and IV) and monoclinic phases (peaks 1 and 3, I and III).

Figure 6a–c show area percent variations for the Zr3*d*, Y3*d* and O1*s* peaks in response to yttria content for the 3–6YSZ samples, respectively. A gradual decrease in the fractions of peaks 1 and 3 for both Zr3*d* and Y3*d* (and fractional increase of peaks 2 and 4) could be found with increasing yttria content. Concurrently, the fractions of peaks I and III for the O1*s* bands decreased at different rates, while those of peaks II and IV gradually increased for the samples in response to temperature increase. Note that for O1*s* sub-bands, the added areal fractions of peaks I and III, S_{I+III}, and of peaks II and IV, S_{II+IV}, represent the monoclinic and tetragonal fractions of the investigated samples, respectively. The variations of the latter parameters with yttria content are shown in Fig. 6d. Figure 6d also shows the fractional variation of hydroxyl-related clusters (i.e., peaks III + IV) and O–Zr clusters (peaks I + II) with yttria content, as obtained from the O1*s* XP spectra of the samples. A fractional decrease (increase) in the total O–H cluster population (O–Zr content) with yttria content could be observed.

Discussion

Examination of yttrium distribution in YSZ ceramics

It is known the mechanical properties of YSZ are strongly influenced by the fabrication procedures, e.g., sintering/calcination parameters [25, 26]. Upon yttria doping, the substitution of yttrium ions, Y^{3+}, for Zr^{4+} induces oxygen vacancies (V_O) in the zirconia lattice for charge compensation and stabilize the

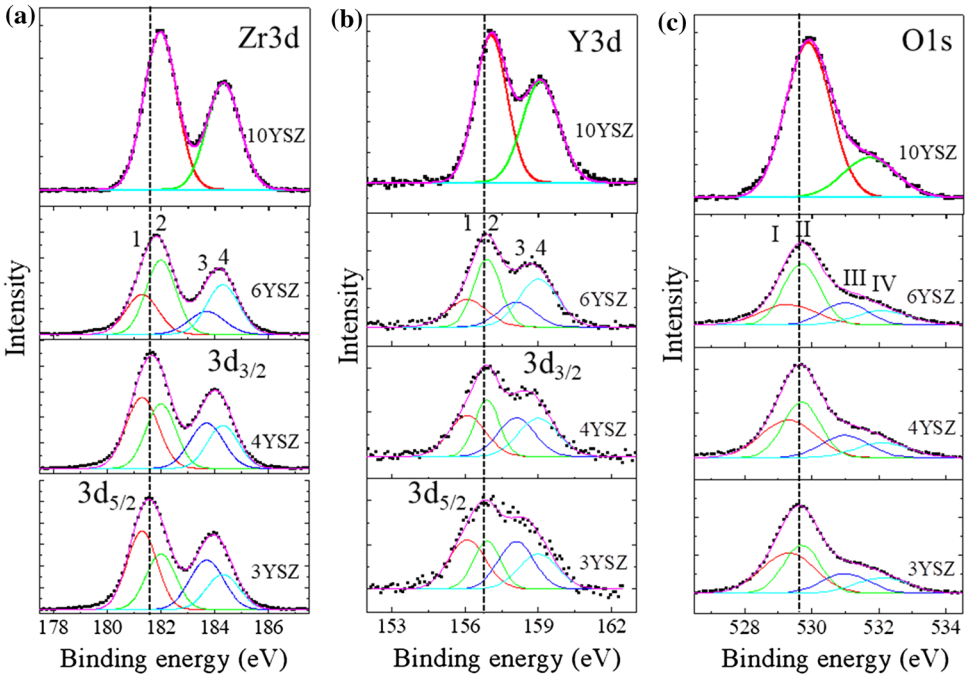

Figure 5 Variations of **a** Zr3*d*, **b** Y3*d*, and **c** O1*s* XP spectra with thermal treatment temperature for the YSZ samples.

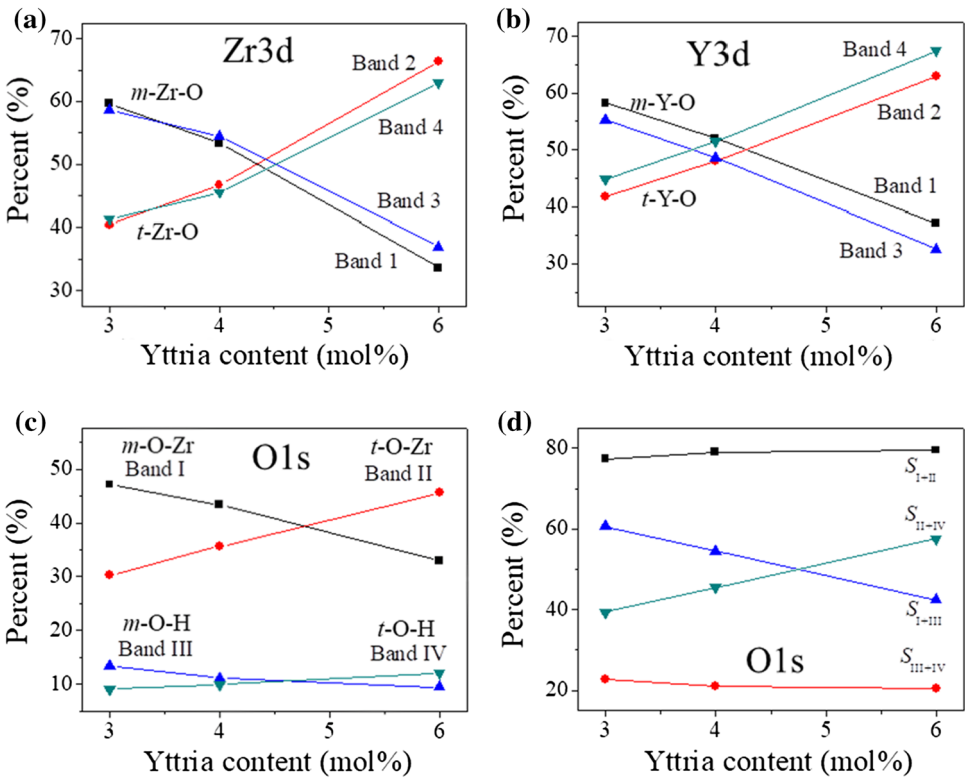

Figure 6 Variations of areal fractions for XPS sub-bands in 3–6YSZ samples with yttria content, as obtained from spectral deconvolution of different XPS lines: **a** Zr3*d*, **b** Y3*d*, **c** O1*s*, and **d** fraction sums, S_{I+II}, S_{III+IV}, S_{I+III}, and S_{II+IV} of O1*s*.

tetragonal lattice. However, even neglecting dopant segregation, the distribution of yttrium atoms is inhomogeneous in YSZ and the Y/Zr ratio vary among different unit cells and different grains. Indeed, experimental analyses by using an electron probe microanalyzer or energy-dispersive spectroscopy in a scanning/transmission electron microscope have revealed an yttrium content below 3 mol% in a considerable number of areas inside the grains in 3Y-TZP materials, although such distribution might strongly depend on fabrication process [14, 27].

In general, for 3Y-TZP, a local area with a lower content of yttria is taken to correspond to a lower stability area, thus more vulnerable to hydrothermal attack. Once a monoclinic nucleus is formed, its further growth can be very fast (exponential increase) [28]. Consequently, the Raman calibrations and imaging proposed in this study provide an effective approach to quantitatively visualizing the local yttrium distribution in *X*YSZ ceramics for better understanding the entire material stability.

According to Fig. 3, both band position and FWHM of the 145 cm^{-1} tetragonal band have shown a dependence on the content of added yttria. Such band alteration is mainly caused by structural distortion in the zirconia lattice induced by the dopant because of both a larger ionic radius and the smaller valence of Y^{3+} ions as compared to Zr^{4+} ions: The higher the dopant content, the more distorted the lattice (as confirmed by the linear shift of the tetragonal XRD peak shown in Fig. 4b), and the more stable the tetragonal structure with a decreased tetragonality (cf. reduction of its FWHM in Fig. 4c). Because the bandwidth is much less altered by the presence of residual stresses generated by phase transformation, a reliable plot of FWHM for the 145 cm^{-1} band versus yttria content at different temperatures could be obtained as shown in Fig. 7a. A linear dependence of FWHM on the added yttria content was found, as follows:

$$\mathrm{FWHM}\left(\mathrm{cm}^{-1}\right) = a * C(\mathrm{Y_2O_3}) + \mathrm{FWHM}_0(T) \qquad (1)$$

where $FWHM_0$ is related to the structural distortion induced by the occurrence of dehydroxylation, and thus a function of temperature (i.e., associated with the amount of hydroxyl or V_O in the lattice) [20]. However, the slope, *a*, was barely affected by thermal treatment temperature ($a \approx 0.3$). Therefore, maps of yttrium distribution in *X*YSZ samples could be retrieved from Raman FWHM maps, according to Eq. (1) as shown for the case of 3YSZ in Fig. 7b. As

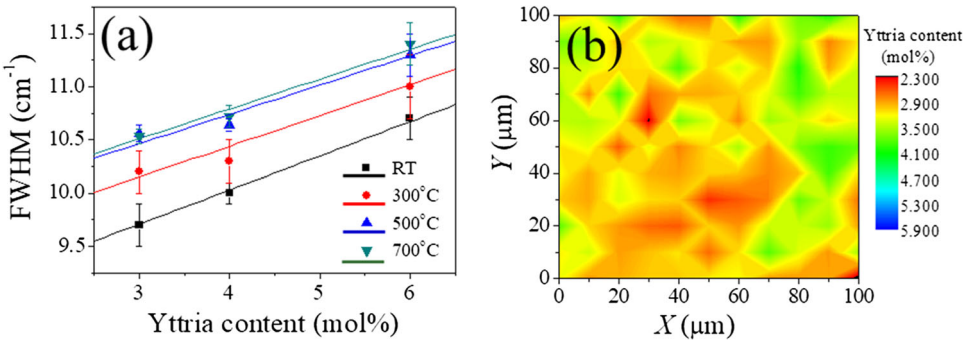

Figure 7 **a** Plots of FWHM of the 145 cm^{-1} Raman mode versus yttria content for the YSZ samples treated at different temperatures, and **b** map of "yttria content" in 3YSZ obtained from the Raman mapping.

mentioned above, for 3YSZ, a lower content of yttria is generally taken to correspond to a lower hydrothermal stability of zirconia. From this viewpoint, the observed variation of yttria content in the Raman map was consistent with that in the V_m map (cf. Fig. 2a, top image): The lower the amount of yttria, the higher the V_m value.

However, it should be noted that here the expression "yttria content" in Fig. 7b does not mean a real presence of yttria grains in the material, but represents an average yttrium content distributed within the measured region that should correspond to the added "yttria content." Moreover, because of the finite Raman probe size (micrometric scale), it shows an average yttrium population inside the probed area, instead of representing a real distribution in the zirconia lattice. Finally, although the samples of higher Y-doping (> 8 mol%) also showed the Raman band at 146 cm^{-1} of the tetragonal (or distorted cubic) phase, the weak signal of this band and the difference in the main structure of zirconia make the application of Eq. (1) infeasible for the cases of high Y-doping.

Despite the above arguments, the detection of yttria content from Raman mapping seemed to be quite efficient, although Eq. (1) might need an additional calibration for YSZ fabricated under different conditions. The method of Raman imaging is fully nondestructive, of relatively fast application, and does not require any sample treatment. It is thus effective in examining local yttrium distribution and local hydrothermal vulnerability in low-content Y-stabilized zirconia ceramics.

Effect of yttria content on thermal stability of zirconia

In our previous papers [19, 20], we have unfolded a significant difference in the kinetics of zirconia polymorphic transformation in different environments and the critical roles played by oxygen vacancy and surface/lattice hydroxyl defects due to the occurrence of distinct off-stoichiometric chemical effects, including hydroxylation, hydroxyl migration, surface reconstruction, and dehydroxylation during treatments.

After sample fabrication, the reaction of the ceramic with adsorbed surface water might cause surface hydroxylation to occur in a humid environment at low temperature. As a result, this leads to the formation of hydroxyl binding to cation ions (Zr, Y) at the very surface of the tetragonal zirconia phase or the incorporation of H_2O molecules into the tetragonal ZrO_2 lattice:

$$Zr(Y)O_2 + H_2O \rightarrow Zr(Y)O(OH)_2 \quad (2)$$

$$H_2O_{(g)} + V_O^{\cdot\cdot} + O_O^x \rightarrow 2(OH)_O^{\cdot} \quad (3)$$

The latter reaction (Eq. 3) causes a reduction in V_O because of the formation of defective protonated hydroxyls and gives a major contribution to the destabilization of the tetragonal polymorph in hydrothermal environment [16, 19]. Moreover, since the presence of oxygen vacancies makes it possible for oxygen ions to move by hopping from vacancy to vacancy in the lattice of yttria-stabilized zirconia [29], a (slow) depth migration of the generated surface hydroxyl into the substrate lattice may also occur to fill the oxygen vacancy in the lattice and to destabilize the tetragonal polymorph, followed by a surface reconstruction [20, 30].

Accordingly, for YSZ samples with surface/lattice hydroxyl defects, dehydroxylation can occur when the sample is subjected to thermal treatments with sufficient thermal energy [20]:

$$2(OH)_O^{\cdot} \rightarrow H_2O_{(g)} + V_O^{\cdot\cdot} + O_O^x \quad (4)$$

The dehydroxylation reaction has a strong dependence on temperature, water pressure, and content of both oxygen vacancy and hydroxyl in the zirconia lattice. In practice, dehydroxylation of the protonated hydroxyl moiety can easily take place in alumina when it is subjected to hydrothermal treatments [31], which may result in a gradual enhancement of the V_O^+ (i.e., oxygen vacancy capturing one electron) cathodoluminescence signal (or F^+ band) with increasing autoclaving time [13].

In the present YSZ samples, given the relatively high hydroxyl content (~ 20%, Fig. 6d) of their lattices and the low water pressure of air, dehydroxylation prevailed upon thermal treatments for all the studied YSZ samples. As a result, the tetragonal phase could be stabilized owing to the generation of oxygen vacancies in the zirconia lattice, and the monoclinic zirconia lattice could even be distorted to re-transform back into the tetragonal phase showing a gradual decrease in V_m with treatment temperature. Moreover, because of the structural "recovery" by reduction of hydroxyl protons in the lattice and the formation of oxygen vacancy, the two polymorphs of zirconia showed a gradual change in both position and FWHM of their Raman bands toward those of the pristine ones [20]. Nevertheless, a clear difference in the rate of reduction of V_m and Raman band shifts with temperature could be found for YSZ samples doped with different yttria contents. This is because the variation in content of oxygen vacancies and hydroxyls is associated with the added yttria content.

Figure 8a, b shows the plots of V_m versus yttria content and V_m versus temperature, respectively, for the 3–6YSZ samples subjected to thermal treatments. As can be seen, with increasing temperature or yttria content, all samples showed a gradual decrease in V_m and the curves seemed to saturate at around 900 °C. The variation of V_m in response to yttria content and temperature can be fitted to a phenomenological equation, as follows:

$$V_m = A * \mathrm{ArcTan}[(B - T)/170] + C \quad (5)$$

where the parameters A, B, and C are yttria content dependent, and can be given as:

$$A = -1.1 * C(Y_2O_3)^{1.1} + 23.8 \quad (6)$$

$$B = 562 * (C(Y_2O_3) - 2.7)^{-0.0351} \quad (7)$$

$$C = 14.2 * (10 - C(Y_2O_3))^{0.35} \quad (8)$$

Upon yttria doping, as mentioned above, oxygen vacancies are generated for charge compensation in the zirconia lattice. Consequently, with increasing yttria content, higher concentrations of oxygen vacancies should be expected, and hydroxylation should be promoted because of a higher probability for hydroxyl to occupy the vacancy sites. In other words, the sample becomes more prone to incorporating hydroxyl in its lattice. However, this is contrary to the present observation that the hydroxyl content decreased with increasing yttria content (cf. Fig. 6d). Because the ionic conductivity of YSZ increases with increasing yttria content and has a maximum at around 8–9 mol% almost independent on temperature [32], the observed decrease in hydroxyl content should not originate from the occurrence of yttrium-incorporation-induced lattice distortion to resist hydroxyl migration, but rather be associated with the formation of stable Y_{Zr}–V_o–Y_{Zr} defect complexes. As the yttria content increases, the probability of forming two neighboring Y_{Zr} defects also increases. These two negatively charged defects can be neutralized by one oxygen vacancy between them. Because of the charge balance, such defect complex can be stable, so that oxygen vacancies are inactivated to accommodate hydroxyl protons. Accordingly, at low yttria contents, the higher hydroxyl content resulted in a higher monoclinic volume fraction, and thus a faster dehydroxylation at high temperature.

Conclusion

In this paper, the effect of yttria content on both structure and thermal stability of zirconia in *X*YSZ samples was investigated by Raman and XPS spectroscopies. Upon increasing yttria content from 3 to 6 mol%, the $t \rightarrow m$ polymorphic transformation induced by surface hydroxyl migration during sample exposure to humid environment was gradually inhibited. V_m values decreased from ~ 56 to ~ 40%, while further exposure of the samples to thermal environments induced an yttria content-dependent reduction in V_m. YSZs doped with yttria content > 8 mol% showed high hydrothermal and thermal stability. The variation of V_m with yttria content and temperature could be interpreted according to a structural model, which takes into account the

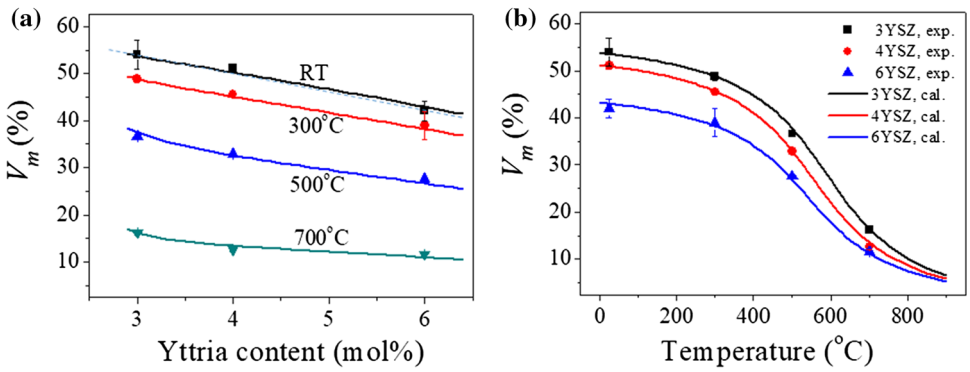

Figure 8 Plots of **a** V_m versus yttria content and **b** V_m versus temperature for the 3–6YSZ samples investigated in this study.

change in content of lattice hydroxyls and oxygen vacancies and the possible formation of stable defect complexes. Upon exploiting the linear dependence of the FWHM of the 145 cm^{-1} tetragonal band with yttria content, Raman imaging appeared to be an effective tool for examining local yttrium distributions in YSZ ceramics.

Compliance with ethical standards

Conflict of interest The authors declare that they have no conflict of interest.

Electronic supplementary material: The online version of this article (https://doi.org/10.1007/s10853-019-04080-9) contains supplementary material, which is available to authorized users.

References

[1] Denry I, Kelly JR (2008) State of the art of zirconia for dental applications. Dent Mater 24:299–307

[2] Zhang F, Vanmeensel K, Batuk M, Hadermann J, Inokoshi M, Meerbeek BV, Naert I, Vleugels J (2015) Highly-translucent, strong and aging-resistant 3Y-TZP ceramics for dental restoration by grain boundary segregation. Acta Biomater 16:215–222

[3] Panadero RA, Roman-Rodriguez JL, Ferreiroa A, Sola-Ruiz MF, Fons-Font A (2014) Zirconia in fixed prosthesis: a literature review. J Clin Exp Dent 6:66–73

[4] Butz B (2011) Yttria-doped zirconia as solid electrolyte for fuel-cell applications: fundamental aspects. Südwestdt Verl. für Hochschulschr, Saarbrücken

[5] Ashton Acton Q (2011) Electrolytes: advances in research and application, Atlanta GA, USA

[6] Hao S-J, Wang C, Liu T-L, Mao Z-M, Mao Z-Q, Wang J-L (2017) Fabrication of nanoscale yttria stabilized zirconia for solid oxide fuel cell. Int J Hydrog Energy 42:29949–29959

[7] Chevalier J, Grandjean S, Kuntz M, Pezzotti G (2009) On the kinetics and impact of tetragonal to monoclinic transformation in an alumina/zirconia composite for arthroplasty applications. Biomaterials 30:5279–5282

[8] McEntire BJ, Enomoto Y, Zhu W, Boffelli M, Marin E, Pezzotti G (2016) Surface toughness of silicon nitride bioceramics: II, comparison with commercial oxide materials. J Mech Behav Biomed Mater 54:346–359

[9] Pezzotti G, Yamada K, Porporati AA, Kuntz M, Yamamoto K (2009) Fracture toughness analysis of advanced ceramic composite for hip prosthesis. J Am Ceram Soc 92:1817–1822

[10] Guo X (2004) Property degradation of tetragonal zirconia induced by low-temperature defect reaction with water molecules. Chem Mater 16:3988–3994

[11] Pinto PA, Colas G, Filleter T, Souza GMD (2016) Surface and mechanical characterization of dental yttria-stabilized tetragonal zirconia polycrystals (3Y-TZP) after different aging processes. Microsc Microanal 22:1179–1188

[12] Butz B, Schneider R, Gerthsen D, Schowalter M, Rosenauer A (2009) Decomposition of 8.5 mol.% Y_2O_3-doped zirconia and its contribution to the degradation of ionic conductivity. Acta Mater 57:5480–5490

[13] Pezzotti G (2013) Advanced materials for joint implants. Pan Stanford, Singapore

[14] Zhang F, Vanmeensel K, Inokoshi M, Batuk M, Hadermann J, Meerbeek BV, Naert I, Vleugels J (2014) 3Y-TZP ceramics with improved hydrothermal degradation resistance and fracture toughness. J Eur Ceram Soc 34:2453–2463

[15] Savin A, Craus M-L, Turchenko V, Bruma A, Dubos P-A, Malo S, Konstantinova TE, Burkhovetsky VV (2015) Monitoring techniques of cerium stabilized zirconia for medical prosthesis. Appl Sci 5:1665–1682

[16] Zhu W, Fujiwara A, Nishiike N, Marin E, Sugano N, Pezzotti G (2018) Transition metals increase hydrothermal stability of yttria-tetragonal zirconia polycrystals (3Y-TZP). J Eur Ceram Soc 38:3573–3577

[17] Butz B, Kruse P, Störmer H, Gerthsen D, Müller A, Weber A, Ivers-Tiffée E (2006) Correlation between microstructure and degradation in conductivity for cubic Y_2O_3-doped ZrO_2. Solid State Ion 177:3275–3284

[18] Sato T, Ohtaki S, Shimada M (1985) Transformation of yttria partially stabilized zirconia by low temperature annealing in air. J Mater Sci 20:1466–1470. https://doi.org/10.1007/BF01026344

[19] Zhu W, Fujiwara A, Nishiike N, Nakashima S, Gu H, Marin E, Sugano N, Pezzotti G (2018) Mechanisms induced by transition metal contaminants and their effect on the hydrothermal stability of zirconia-containing bioceramics: an XPS study. Phys Chem Chem Phys 20:28929–28940

[20] Zhu W, Nakashima S, Matsuura M, Gu H, Marin E, Pezzotti G (2019) Raman and X-ray photoelectron spectroscopic characterization of thermal stability of 3 mol% yttria stabilized zirconia ceramics. J Eur Ceram Soc 39:4928–4935. https://doi.org/10.1016/j.jeurceramsoc.2019.06.056

[21] Katagiri G, Ishida H, Ishitani A, Masaki T (1988) Direct determination by a Raman microprobe of the transformation zone size in Y_2O_3 containing tetragonal ZrO_2 polycrystals. Adv Ceram 24:537–544

[22] Chevalier J, Deville S, Münch E, Jullian R, Lair F (2004) Critical effect of cubic phase on aging in 3 mol% yttria-stabilized zirconia ceramics for hip replacement prosthesis. Biomaterials 25:5539–5545

[23] Witz G, Shklover V, Steurer W, Bachegowda S, Bossmann H-P (2007) Phase evolution in yttria-stabilized zirconia thermal barrier coatings studied by rietveld refinement of X-ray powder diffraction patterns. J Am Ceram Soc 90:2935–2940

[24] Asadikiya M, Sabarou H, Chen M, Zhong Y (2016) Phase diagram for a nano-yttria-stabilized zirconia system. RSC Adv 6:17438–17445

[25] Pandey AK, Biswas K (2014) Effect of agglomeration and calcination temperature on the mechanical properties of yttria stabilized zirconia. Ceram Int 40:14111–14117

[26] Madeira S, Buciumeanu M, Carvalho O, Silva FS (2019) Influence of sintering pressure on the microstructure and tribological properties of low temperature fast sintered hot-pressed Y-TZP. Ceram Int 45:5883–5893

[27] Basu B, Balani K (2011) Advanced structural ceramics. Wiley, Hoboken

[28] Chevalier J, Gremillard L, Deville S (2007) Low-temperature degradation of zirconia and implications for biomedical implants. Annu Rev Mater Res 37:1–32

[29] Ahamer C, Opitz AK, Rupp GM, Fleig J (2017) Revisiting the temperature dependent ionic conductivity of yttria stabilized zirconia (YSZ). J Electrochem Soc 164:F790–F803

[30] Merle-Mejean T, Barberis P, Othmane SB, Nardou F, Quintard PE (1998) Chemical forms of hydroxyls on/in zirconia: an FT-IR study. J Eur Ceram Soc 18:1579–1586

[31] Balint I, Springuel-Huet M-A, Aika K-I, Fraissard J (1999) Evidence for oxygen vacancy formation in HZSM-5 at high temperature. Phys Chem Chem Phys 1:3845–3851

[32] Yanagida H, Koumoto K, Miyayama M (1996) The chemistry of ceramics. Wiley, New York